Material nonlinearities yield doubly negative holey metamaterials

Shresht Jain [a], Finn Box [a], Chris Johnson [b], Draga Pihler-Puzović [a,*]

[a] *Department of Physics & Astronomy and Manchester Centre for Nonlinear Dynamics, University of Manchester, Oxford Road, M13 9PL, Manchester, UK*
[b] *Department of Mathematics and Manchester Centre for Nonlinear Dynamics, University of Manchester, Oxford Road, M13 9PL, Manchester, UK*

ARTICLE INFO

ABSTRACT

Mechanical metamaterials with negative stiffness and negative Poisson's ratio are exciting prospects for advanced material design. A plastic column with a series of periodically-spaced holes exhibits both of these properties when buckled under compression. In this paper, the behaviour of such a column under compression is measured experimentally and described with a simple mathematical model. This model predicts the compression, buckling and post-buckling behaviour of the entire column from the mechanical response of the thin ligaments of material that form the column's microarchitecture to compression, rotation and shear forces, which are characterised experimentally, The softening behaviour in holey columns beyond the critical level of compression for pattern transformation is shown to be due to material constitutive nonlinearities in the rotation and shear response of the microarchitecture. Geometric perturbations to the columns can cause the observed pattern to change, but result in approximately the same force–displacement measurements as for the column with perfect geometry. This approach provides a useful framework to study systems where both geometric and material nonlinearities underpin observed phenomena.

1. Introduction

The extraordinary properties of mechanical metamaterials are dictated by the deformation of their microarchitecture. Typically, these systems are soft, and their macromechanics are assumed to be governed by the nonlinear structural geometry generated by a repeating microarchitecture which deforms in a reversible way. In recent years, however, tailoring of material nonlinearities has unlocked additional functionality. Metamaterials manufactured from complex fluids are a prime example. Viscoelastic metamaterials exhibit strain-rate dependence [1,2], have temperature dependent properties that enable a greater degree of post-fabrication tunability [3], and can even improve sensory perception [4]. Metamaterials made from dense suspensions can switch between shear-thickened, high-viscosity and dethickened, low-viscosity states in response to acoustic actuation, and be engineered to display negative viscosity [5]. Granular metamaterials can develop rheological 'point' defects [6] that affect wave propagation through them.

In some instances, a sound understanding of how material nonlinearities affect the deformation of a metamaterial is a prerequisite for their practical application. A case in point is the use of hard metamaterials as shock absorbers or crumple zones [7,8], i.e., structures that are designed to deform plastically and absorb mechanical energy in the process [9]. Widespread adoption of metamaterial designs for crumple zones in the automotive industry, for example, will demand materials that are high strength and resistant to degradation. Hard auxetic metamaterials [10], in particular, offer great potential since they contract laterally, rather than expanding, under compression; integral to their performance are the irreversible deformations which occur when applied stresses exceed the yield stress of the (meta)material and result in a nonlinear material response to deformation.

Here, we describe how material nonlinearities alter the buckling behaviour of the 'holey column', a quintessential class of mechanical metamaterial containing a periodic array of circular holes (Fig. 1a). Holey columns and other cellular solids of the same type exhibit negative Poisson's ratio behaviour: beyond a critical compressive strain, the columns buckle, and the holes undergo a pattern transformation from circular to neighbouring, orthogonal ellipses that results in lateral contraction at the macroscale (Fig. 1b, see also [10,11]). As one of the early examples of an artificial, mechanical metamaterials [11–17], they remain a cornerstone of research in the field because their simple geometry permits analytical progress and their macroscopic properties can be easily tailored through e.g., alterations to the hole size and spacing [16,18]. Traditionally, research focused on the role of geometrical nonlinearities on pattern transformation and associated emergent properties, while the material properties of holey

---

* Corresponding author.
E-mail address: draga-pihler-puzovic@manchester.ac.uk
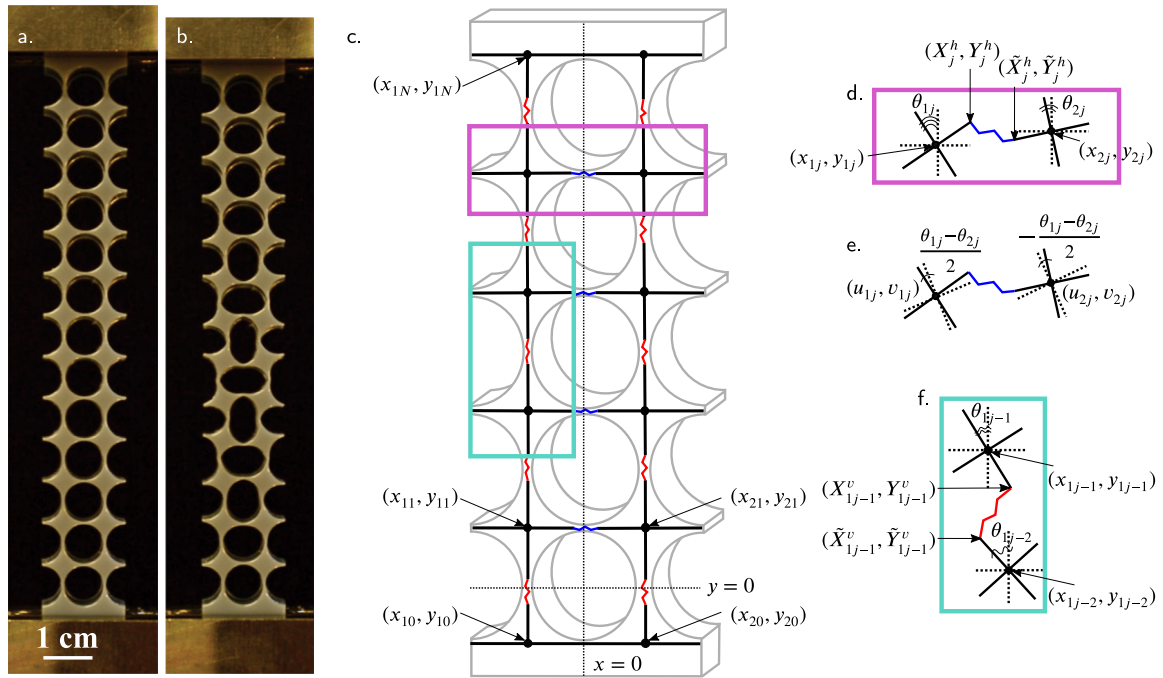(D. Pihler-Puzović).

Fig. 1. Deforming metamaterials with constitutive nonlinearities. a–b. A holey column (made from polylactic acid (PLA) using a 3D printer) under compression. For sufficient applied load, buckling of the thin ligaments surrounding holes induces pattern switching (from circles to orthogonal ellipses). c–f. Schematic diagrams of our deconstructed model system comprising rigid joints and flexible spring-like ligaments that are connected in series and orientated in the horizontal (purple box) and vertical (green box) components. Each rigid piece is defined with the following degrees of freedom $\{x_{ij}, y_{ij}, \theta_{ij}\}$. d. The coordinates of the left-edge and right-edge of a horizontal ligament are $\{X_j^h, Y_j^h\}$ and $\{\tilde{X}_j^h, \tilde{Y}_j^h\}$, respectively. e. Illustration of the transformation from Cartesian coordinates to the frame of reference in which compression of each ligament occurs along one principal axis and shearing along the other, for a horizontal component. f. Similarly to figure d, the top and bottom edges of vertical ligaments are defined by $\{X_{ij}^v, Y_{ij}^v\}$ and $\{\tilde{X}_{ij}^v, \tilde{Y}_{ij}^v\}$, respectively.

structures were either assumed linearly elastic, or remained at the periphery of scientific exploration [19–22].

The novelty in our approach is to consider both geometrical nonlinearities and nonlinear constitutive relations between deformations and applied loads. The model presented here links the nonlinear mechanics of the microarchitecture to the macroscale behaviour of non-elastic holey columns. Although the influence of nonlinearities on the onset of pattern transformation is small, they can significantly affect the post-buckling bifurcation structure. Our findings shed light on recent experimental reports of metamaterials [10] made from common metals and plastics that exhibit both a negative Poisson's ratio and negative stiffness following pattern transformation (i.e., they are '*doubly negative*' [23]).

Metamaterials that demonstrate negative stiffness [24], negative compressibility [25] and other advanced functionalities – such as tunable, multistage [26] and multi-directional [27] stiffness – offer great potential for energy absorption and vibration isolation applications, but typically their design has relied on geometric nonlinearities that arise during deformation. Extreme damping and negative stiffness have been reported in composite materials that contain either negative compressibility inclusions within a stiff matrix [28–32] (where elastic energy is stored in the inclusions) or microscale, bucklable structures embedded in a viscoelastic matrix [33] (where energy is instead dissipated by amplifying linear strains in the host material), suggesting that negative stiffness is a common property of composite materials with nonlinear constitutive relations.

Herein, we show that non-compound metamaterials can also exhibit negative stiffness, providing their material properties are constitutively nonlinear, and reveal the post-buckling bifurcation structure responsible for the emergent negative stiffness. First, we characterise the micromechanics of our metamaterial,

a hard holey column, by measuring the deformation of its individual structural elements to applied compression, shear and rotation. We then simulate the behaviour of our columns under compression using a network model with nonlinear constitutive behaviour extracted from measurements of structural elements, and compare these simulation results to experiments. Finally, we discuss the role of nonlinear rotation and shearing, and that of geometrical imperfections, on the magnitude of peak force at the onset of buckling and the post-buckling negative stiffness.

2. Experiments

2.1. Materials and methods

Compressive testing was performed on holey columns (Fig. 1a) and microstructural elements made from plastic. All samples were fabricated in polylactic acid (PLA) plastic (VeroBlue, Stratasys Ltd.) using a 3D printer (Objet30 Pro, Stratasys Ltd). The measured Young's modulus of the PLA was 2.0 GPa.

Holey columns consisted of repeated structural elements of half-length $l = 4.05$ mm, half-width $w = 4.05$ mm and depth $d = 12.7$ mm, shown in Fig. 2a, so that the samples had a hole diameter $D = 7.7$ mm, and the hole centres were $2 \times l = 8.1$ mm apart. A length $l_{ends} = 12$ mm of solid material, free from holes, was left on the top and bottom of the structure, and placed inside custom-built adaptors to prevent sliding of the samples during testing. The error on all geometric parameters was within 0.5% of the numbers quoted above.

The structural elements used to measure the micromechanical response to shear and rotation are shown in Figs. 2a.ii & a.iii. The deforming parts of the microstructures were geometrically identical to the one depicted in Fig. 2a.i., i.e. their dimensions were the same as found in the microarchitecture of our holey
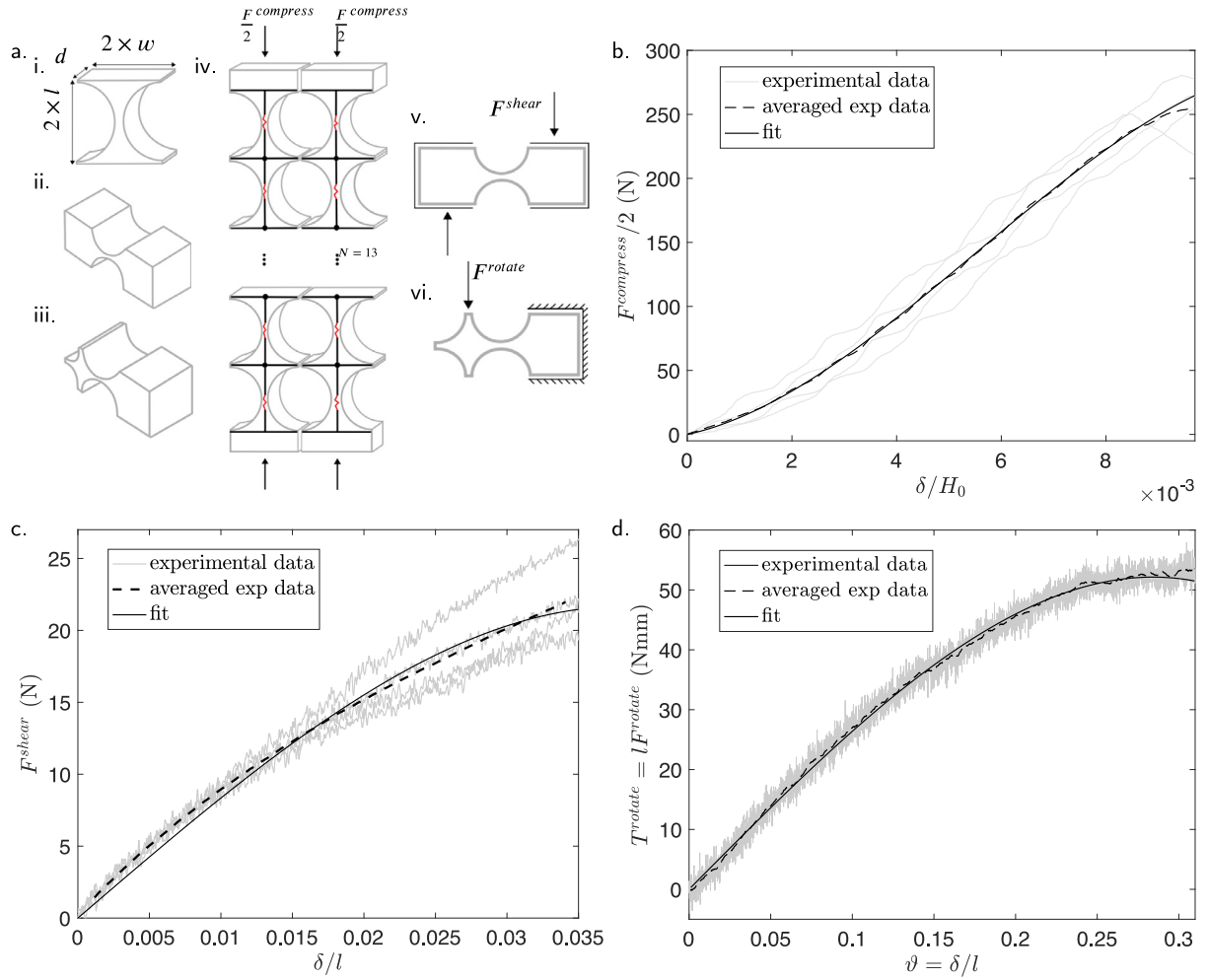
Fig. 2. Micromechanics. a. Schematic illustration of (i) the basic structural element of depth d, width $2 \times w$ and length $2 \times l$ that repeats throughout the column, and experimental samples used to measure the (ii) shear and (iii) rotational response of the microarchitecture [10]. Schematic illustration of experiments used for measuring the (iv) compression, (v) shear and (vi) rotation response of the basic structural elements. b. Half of the measured force, $F^{compress}/2$, as a function of nondimensional vertical displacement, δ/H_0, from compression experiments as in a.iv with holey columns of initial height, H_0, and $N = 13$ holes prior to buckling; experimental data is fitted with Eq. (2). c. Measured force, F^{shear}, as a function of nondimensional vertical displacement, δ/l, from shear experiments as in a.v with samples from a.ii; experimental data is fitted with Eq. (4). d. Measured torque, $T^{rotate} = lF^{rotate}$, as a function of angular rotation, $\vartheta = \delta/l$, in rotation experiments as in a.vi with samples from a.iii; experimental data is fitted with Eq. (6). Figures b–d show both raw (faint lines) and averaged (dashed line) experimental data; fits (solid lines) are done with the latter.

columns. However, the geometry outside the deforming region was adapted to allow the elements to be attached to the structural testing station using custom-built adaptors, and then subjected to these specific deformation modes (Figs. 2a.v & a.vi, respectively).

Force–displacement data was acquired using a Universal Testing System (5569, Instron) by compressing samples at rates in the range of 0.001–8.5 mm/s. Five experimental runs were repeated per set of parameters, and a new sample was produced for each experimental run since each sample deformed plastically during testing. For each level of displacement, the force measured from multiple experimental runs is averaged, with the error on each point corresponding to the standard deviation of the data.

2.2. Micromechanics

The pre-buckling deformation of compressed holey columns is primarily accommodated through the compression of vertically-oriented structural elements, shown in Fig. 2a.i. In order to extract the individual response of these elements to compression, we assume that prior to buckling, the holey column is comprised of two stacks of such structures connected in parallel (see

Fig. 2a.iv). Force–displacement measurements, e.g., in Fig. 2b for a holey column with $N = 13$ holes, suggest a nonlinear response to compression. Hence, the compression energy of an individual structural element depends on the amount of compression δ as

$$C(\delta) = \mathcal{C}_2\delta^2 + \mathcal{C}_3|\delta|^3 + \mathcal{C}_4\delta^4, \tag{1}$$

where $\mathcal{C}_2$ is the Young's modulus for small displacements. Prior to buckling, this compression energy determines the force–displacement behaviour of the entire column, with the force applied when a holey column with N holes is compressed by a distance δ being

$$F^{compress} = 2C'(\delta/N). \tag{2}$$

Experimental measurements of the force versus displacement shown in Fig. 2b for $N = 13$ are typical for holey columns prior to buckling, and are used to extract $\mathcal{C}_2$, $\mathcal{C}_3$ and $\mathcal{C}_4$ by fitting (2) to the averaged experimental data in Fig. 2b. The results of this fitting are also shown in Fig. 2b. The compression coefficients $\mathcal{C}_2$, $\mathcal{C}_3$ and $\mathcal{C}_4$ are determined to be 550.6 ± 100.7 N/mm, 23.18 ± 0.76 kN/mm^2 and -1293.4 ± 6.5 kN/mm^3, respectively, and are used in the theoretical model below to predict the post-buckling

behaviour of the holey column with $N = 13$ holes, and the pre- and post-buckling behaviours of columns with $N \neq 13$ holes.

The energy of an individual structural element under shear must be, by symmetry, an even function, approximated here by the first two terms of a power series,

$$S(\delta) = \mathcal{S}_2 \delta^2 + \mathcal{S}_4 \delta^4. \tag{3}$$

Thus, for a structural element subject to shear, the measured force is related to displacement through

$$F^{shear} = 2\mathcal{S}_2 \delta + 4\mathcal{S}_4 \delta^3, \tag{4}$$

where the vertical displacement δ is applied as shown in Fig. 2.a.v, and the corresponding force F^{shear} is measured. The resulting force–displacement data for different experiments and their average are shown in Fig. 2.c. As before, the polynomial (4) is fitted to experimental data (Fig. 2.c), with coefficients $\mathcal{S}_2 = 105.5 \pm 1.7$ N/mm and $\mathcal{S}_4 = -740.9 \pm 50.5$ N/mm^3.

The rotational (bending) energy of the structural elements must also be an even function of the deformation. In experiments (Fig. 2.a.vi) this is measured by applying a vertical displacement δ and measuring the corresponding force F^{rotate}, so the angle ϑ can be approximated as δ/l, where, as before, l is the undeformed half-length of the microarchitecture. As with shearing, the first two terms of a power series approximate the bending response,

$$R(\vartheta) = \mathcal{R}_2 \vartheta^2 + \mathcal{R}_4 \vartheta^4, \tag{5}$$

such that the torque on the tested structural element is related to the measured force–displacement via

$$T^{rotate} = F^{rotate} l = 2\mathcal{R}_2 \vartheta + 4\mathcal{R}_4 \vartheta^3 = 2\mathcal{R}_2 \frac{\delta}{l} + 4\mathcal{R}_4 \left(\frac{\delta}{l}\right)^3. \tag{6}$$

Again, coefficients $\mathcal{R}_2$ and $\mathcal{R}_4$ are obtained by fitting (6) to the experimental force–displacement data (Fig. 2.d), resulting in $\mathcal{R}_2 = 142.07$ N mm/rad and $\mathcal{R}_4 = -388.34$ N mm/rad^3, respectively.

3. Theory

We model the holey columns as series of rigid sections that are connected by thin flexible ligaments (Fig. 1.c–f), an approach justified by the thin hourglass-shaped region of flexible material between adjacent holes [20]. Such ligaments can be modelled by constitutively linear rotation and translation springs [22,34], but here, to recreate the post-buckling softening observed in hard, holey columns, we must turn to models of ligament deformation with a nonlinear constitutive response.

3.1. The elastic column model

The total elastic energy of the column is a sum over the elastic energies of each flexible ligament, each of which has contributions from compression, shear and rotational deformations of that ligament. In this subsection, these ligament deformations are defined in terms of the position and rotation angle of each rigid section of the column. The total elastic energy (28) is written in terms of these unknowns, which, when minimised, gives the equilibrium states of the column.

The geometry of the holey column is described using a Cartesian coordinate system centred on the bottom hole of the column (Fig. 1.c). The rigid sections are formed from the thick regions of elastic material of half-length l_{ij} and half-width w_{ij}, centred at (x_{ij}, y_{ij}), where $i = 1, 2$ and $0 \leq j \leq N$ for the column with N holes. Thus, the height of the column can be determined as

$$H_0 = l_{i0} + 2 \sum_{j=1}^{N-1} l_{ij} + l_{iN}, \text{ for } i = 1 \text{ or } i = 2. \tag{7}$$

If the column is compressed by δ, then the total height of the column changes to

$$H = H_0 - \delta. \tag{8}$$

The rotation of rigid segments is described by angles θ_{ij} measured anticlockwise from the vertical axis as illustrated in Figs. 1d & 1f.

There are $N - 1$ horizontally-oriented flexible ligaments in total (shown with blue springs in Figs. 1c & 1d). The deformation of these ligaments is the difference in position between their left and right edges, which have coordinates

$$\left.\begin{array}{l} X_j^h = x_{1j} + w_{1j} \cos\theta_{1j}, \\ Y_j^h = y_{1j} + w_{1j} \sin\theta_{1j}, \end{array}\right\} \quad \text{for } 1 \leq j \leq N - 1, \tag{9}$$

for the left-hand edge and

$$\left.\begin{array}{l} \tilde{X}_j^h = x_{2j} - w_{2j} \cos\theta_{2j}, \\ \tilde{Y}_j^h = y_{2j} - w_{2j} \sin\theta_{2j}, \end{array}\right\} \quad \text{for } 1 \leq j \leq N - 1 \tag{10}$$

for the right-hand edge. The energy associated with the deformation of the horizontally-oriented flexible ligaments is then

$$E^h = \sum_j^{N-1} E^h(X_j^h - \tilde{X}_j^h, Y_j^h - \tilde{Y}_j^h, \theta_{1j} - \theta_{2j}; w_{1j}, w_{2j}), \tag{11}$$

The total number of vertically-oriented flexible ligaments (shown with red springs in Figs. 1c & 1f) is $2 \times N$, and we refer to each one of them using two indices (i, j). The deformation of the (i,j)th ligament can be described using

$$\left.\begin{array}{l} X_{ij}^v = x_{ij} + l_{ij} \cos\theta_{ij}, \\ Y_{ij}^v = y_{ij} - l_{ij} \sin\theta_{ij}, \end{array}\right\} \quad \text{for } \begin{array}{l} 1 \leq j \leq N - 1, \\ i = 1, 2, \end{array} \tag{12}$$

for coordinates of its top edge, and

$$\left.\begin{array}{l} \tilde{X}_{ij}^v = x_{ij-1} - l_{ij-1} \sin\theta_{ij-1}, \\ \tilde{Y}_{ij}^v = y_{ij-1} + l_{ij-1} \cos\theta_{ij-1} \end{array}\right\} \quad \text{for } \begin{array}{l} 2 \leq j \leq N, \\ i = 1, 2, \end{array} \tag{13}$$

for coordinates of its bottom edge. The rigid sections next to the boundaries of the holey column differ from the rest of the rigid sections because they do not rotate, so the coordinates of the vertically-oriented flexible ligaments adjacent to these boundaries are

$$\begin{array}{l} \tilde{X}_{11}^v = -w_{11} \quad \text{and} \quad \tilde{X}_{21}^v = w_{21}, \\ \tilde{Y}_{11}^v = 0 \quad \text{and} \quad \tilde{Y}_{21}^v = 0 \end{array} \tag{14}$$

at the bottom boundary,

$$\begin{array}{l} X_{1N}^v = -w_{1N} \quad \text{and} \quad X_{2N}^v = w_{2N}, \\ Y_{1N}^v = H - l_{1N} \quad \text{and} \quad Y_{2N}^v = H - l_{2N} \end{array} \tag{15}$$

at the top boundary, respectively. The energy associated with the deformation of the vertically-oriented flexible ligaments can be expressed as

$$E^v = \sum_{i=1}^2 \sum_{j=1}^N E^v(X_{ij}^v - \tilde{X}_{ij}^v, Y_{ij}^v - \tilde{Y}_{ij}^v, \theta_{ij} - \theta_{ij-1}; l_{ij}, l_{ij-1}). \tag{16}$$

As the holey column deforms, each ligament can, in principle, compress, shear and rotate, and we assume that the former two types of responses decouple along the principal axes of the individual rigid segments. Each segment is associated with its principal coordinate system given by

$$u_{1j} = x_{1j} \cos(\phi_j) + y_{1j} \sin(\phi_j), \tag{17}$$

$$v_{1j} = -x_{1j} \sin(\phi_j) + y_{1j} \cos(\phi_j), \tag{18}$$

if the segment is on the left-hand side of the holey column, and by

$$u_{2j} = x_{2j} \cos(-\phi_j) + y_{2j} \sin(-\phi_j), \tag{19}$$

$$v_{2j} = -x_{2j} \sin(-\phi_j) + y_{2j} \cos(-\phi_j), \tag{20}$$

if the segment is on the right-hand side of the holey column, respectively, where the (x, y)-coordinate system is rotated by an angle

$$\phi_j = \frac{\theta_{1j} + \theta_{2j}}{2}, \tag{21}$$

see Figs. 1e. Thus, the edge coordinates of the horizontally-oriented flexible ligament can be expressed as

$$\begin{aligned} X_j^h &= X_j^h(x_{1j}, \theta_{1j}; w_{1j}) \\ &= X_j^h(x_{1j}(u_{1j}, v_{1j}, \phi_j), \theta_{1j}; w_{1j}) \\ &= U^v(u_{1j}, v_{1j}, \phi_j, \theta_{1j}; w_{1j}), \end{aligned}$$

and become

$$\left.\begin{aligned} X_j^h(x_{1j}, \theta_{1j}; w_{1j}) &= U_j^h(u_{1j}, v_{1j}, \phi_j, \theta_{1j}; w_{1j}), \\ Y_j^h(y_{1j}, \theta_{1j}; w_{1j}) &= V_j^h(u_{1j}, v_{1j}, \phi_j, \theta_{1j}; w_{1j}), \end{aligned}\right\}$$
$$\text{for} \quad 1 \leq j \leq N - 1, \tag{22}$$

for the left-hand side edge coordinates, and

$$\left.\begin{aligned} \tilde{X}_j^h(x_{2j}, \theta_{2j}; w_{2j}) &= \tilde{U}_j^h(u_{2j}, v_{2j}, \phi_j, \theta_{2j}; w_{2j}), \\ \tilde{Y}_j^h(y_{2j}, \theta_{2j}; w_{2j}) &= \tilde{V}_j^h(u_{2j}, v_{2j}, \phi_j, \theta_{2j}; w_{2j}), \end{aligned}\right\}$$
$$\text{for} \quad 1 \leq j \leq N - 1, \tag{23}$$

for the right-hand side edge coordinates, respectively. Then the energy associated with the deformation of the horizontally-oriented flexible ligaments can be rewritten as

$$E^h = \sum_{j=1}^{N-1} C(U_j^h - \tilde{U}_j^h) + S(V_j^h - \tilde{V}_j^h) + R(\theta_{1j} - \theta_{2j}), \tag{24}$$

where C, S, R are contributions to the energy due to compression, shear and rotation, defined in (1), (3) and (5), respectively. Similarly, for the edge coordinates of the vertically-oriented flexible ligament

$$\begin{aligned} X_{ij}^v &= X_{ij}^v(x_{ij}, \theta_{ij}; l_{ij}) \\ &= X_{ij}^v(x_{ij}(u_{ij}, v_{ij}, \phi_j), \theta_{ij}; l_{ij}) \\ &= U_{ij}^v(u_{ij}, v_{ij}, \phi_j, \theta_{ij}; l_{ij}). \end{aligned}$$

Hence, the top edge coordinates of the vertically-oriented elastic ligament become

$$\left.\begin{aligned} X_{ij}^v(x_{ij}, \theta_{ij}; l_{ij}) &= U_{ij}^v(u_{ij}, v_{ij}, \phi_j, \theta_{ij}; l_{ij}), \\ Y_{ij}^v(y_{ij}, \theta_{ij}; l_{ij}) &= V_{ij}^v(u_{ij}, v_{ij}, \phi_j, \theta_{ij}; l_{ij}), \end{aligned}\right\}$$
$$\text{for} \quad 1 \leq j \leq N - 1 \quad \& \quad i = 1, 2, \tag{25}$$

while the bottom edge coordinates become

$$\left.\begin{aligned} \tilde{X}_{ij}^v(x_{ij-1}, \theta_{ij-1}; l_{ij-1}) &= \tilde{U}_{ij}^v(u_{ij-1}, v_{ij-1}, \phi_j, \theta_{ij-1}; l_{ij-1}), \\ \tilde{Y}_{ij}^v(y_{ij-1}, \theta_{ij-1}; l_{ij-1}) &= \tilde{V}_{ij}^v(u_{ij-1}, v_{ij-1}, \phi_j, \theta_{ij-1}; l_{ij-1}), \end{aligned}\right\}$$
$$\text{for} \quad 2 \leq j \leq N \quad \& \quad i = 1, 2, \tag{26}$$

and the energy associated with the deformation of the vertically-oriented flexible ligaments is

$$E^v = \sum_{i=1}^{2} \sum_{j=1}^{N-1} C(V_{ij}^v - \tilde{V}_{ij}^v) + S(U_{ij}^v - \tilde{U}_{ij}^v) + R(\theta_{ij} - \theta_{ij-1}). \tag{27}$$

Adding (24) and (27), we obtain the total energy of the holey column

$$E = E^h + E^v. \tag{28}$$

For each level of compression δ, the equilibrium states of the holey column defined by the particular $\{x_{ij}, y_{ij}, \theta_{ij}\}$ can be solved for by minimising this energy, i.e.

$$\frac{\partial E}{\partial \xi} = 0, \tag{29}$$

where $\xi = \{x_{ij}, y_{ij}, \theta_{ij}\}$.

3.2. Numerical solution

Once formulated, the algebraic system (29) is solved using the Newton–Raphson method, and parametric continuation is used to compute equilibrium solutions for a range of compression δ. The compression force is computed from a finite-difference derivative of the energy associated with each equilibrium,

$$F = \frac{E(\delta + \Delta\delta) - E(\delta)}{\Delta\delta}. \tag{30}$$

Alternatively, the force can be imposed by applying a weight F to the top of the column ($z = H$). The energy of the holey column (28), is then

$$\tilde{E} = E + F \times H, \tag{31}$$

where the second term corresponds to the potential energy due to the weight. In this formulation, F is imposed, and the compression δ is an additional unknown that we solve for together with the column geometry ξ. Applying the method of Lagrange multipliers to (31), we again obtain the Eqs. (29), alongside a new equation

$$\frac{\partial E}{\partial \delta} = F. \tag{32}$$

As above, we then proceed to perform parametric continuation in force.

Bifurcations are identified by monitoring when an eigenvalue of the Jacobian of (29) changes sign during continuation. At a bifurcation, perturbing the initial guess of the Newton–Raphson solve with a small multiple of the corresponding eigenvector allows continuation along a chosen solution branch.

3.3. Modelling geometric imperfections

The majority of our results are computed using holey columns in which the structural elements that form them have the same half-lengths $\{l_{ij}\} = l$ and half-widths $\{w_{ij}\} = w$. In practice, however, all mechanical metamaterials are inherently imperfect because of limitations in the fabrication processes [35], so accounting for geometric uncertainties is useful in their design and characterisation [36]. Here, this is examined theoretically by creating columns with $l_{ij} = l + \epsilon \rho_{ij}$ and $w_{ij} = w + \epsilon \tilde{\rho}_{ij}$, where ρ_{ij} and $\tilde{\rho}_{ij}$ are randomly chosen factors for the columns lengths and widths, drawn from intervals $[-l, l]$ and $[-w, w]$, respectively, with a uniform probability distribution. These are scaled by the scaling amplitude $\epsilon = 0.005$, chosen to reflect the size of typical imperfection in our experiments (Section 2.1). Their role was studied using 50 imperfect columns.

4. Results

4.1. Macromechanics

The macromechanical response of holey columns to compression is summarised in Fig. 3a, which shows how the
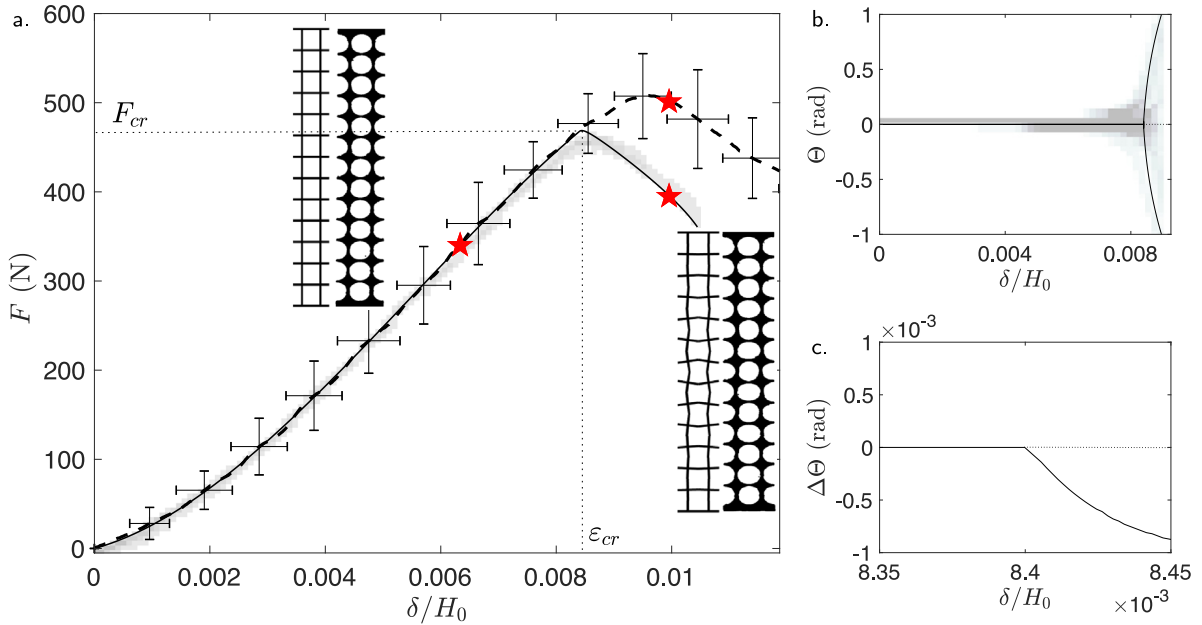
Fig. 3. The macromechanics and observed buckling modes. a. The macromechanical response (i.e., measured force) of a holey, plastic column with $N = 13$ holes to applied compressive strain $\varepsilon = \delta/H_0$ and observed buckling mode. The dashed line and errorbars represent the average and standard deviation of experimental measurements, the solid black line represents numerical predictions for the perfect column while the shaded regions correspond to data obtained in 50 numerical simulations with geometrical imperfections (with denser data regions being darker). Examples of predicted and observed states, pre- and post-buckling, are shown as insets and correspond to values of applied strain indicated by the red stars. Also indicated are the critical strain ε_{cr} and load F_{cr} for buckling obtained in simulations with the perfect column. b. The global orientation of holes, Θ, measured as a function of compressive strain shows how the trivial compression branch, $\Theta = 0$, bifurcates into two different alternating modes when $\varepsilon = \varepsilon_{cr}$. As in figure a, the solid black line is for the perfect column while faint markers show the influence of geometrical imperfections on observed mode. c. The difference between the branches in figure b which correspond to different global hole orientations of the perfect column, $\Delta\Theta$, as a function of compressive strain in the region close to the critical strain ε_{cr} above which $\Delta\Theta < 0$.

measured force varies as a function of applied compressive strain for columns with $N = 13$ holes. The mean of the experimental data and the corresponding errors are shown using dashed line with error bars, while the predictions of the theoretical model from Section 3.1 for the perfect column are illustrated with the solid line. The pattern transition due to the column buckling is characterised by the peak in the measured force F_{cr} at the applied compressive strain ε_{cr}. The agreement between the experimental and theoretical curves is good, particularly in their overall shape, with the predicted values for the critical force and compressive strain to within 9% of each other. Perturbations to the sample geometry make the bifurcation at ε_{cr} imperfect (shading in Fig. 3a), and decrease the peak stress by $\sim$5% for each percent in the geometric perturbation, but otherwise do not dramatically change the force–strain relation of the system, compared to the case of a perfect column.

For representative values of the applied strain before and after the pattern transition, indicated with the star markers, also shown are column states obtained experimentally and in our model with the perfect column. Again, the agreement between the two is good, e.g. beyond the onset of buckling, the middle (elliptical) hole is oriented vertically so that the vertical ligaments surrounding it are closer to each other than the horizontal ligaments. An alternative buckled state with the middle (elliptical) hole oriented horizontally, with a nearly identical force–displacement relation, is also predicted by the model. Both buckled states can be traced by measuring the total rotation in the column using a measure of the global orientation of holes that is positive for the buckled state with the middle hole oriented vertically, and negative for the buckled state with the middle hole oriented horizontally, such as $\Theta = \sum_{k=1}^{N}(-1)^k(\theta_{2k} - \theta_{1k})$. Fig. 3b shows the variation of Θ with the compressive strain near the bifurcation point for the perfect column (solid line) and 50 imperfect columns (shaded regions). The pattern transition is not

symmetry-breaking, as both buckled states maintain both top-bottom and left–right reflection symmetries of the undeformed column. Indeed the two post-buckling branches are not perfectly symmetric, as shown in Fig. 3c where the sum $\Delta\Theta$ of the top and bottom branches for the perfect column from Fig. 3c is plotted. For perfect columns with an odd number of holes, the buckling occurs through a transcritical bifurcation, with a nearby limit point [19], that for $N = 13$ occurs at a value of δ/H_0 only $\sim$10^{-6}% less than that of the bifurcation. The two buckled states follow almost identical force–displacement curves, though one has positive Θ and one has negative Θ. In practice, even tiny geometric perturbations to the shape of the holey column (and likely other experimental perturbations not studied here), cause the bifurcation to become imperfect, with either the positive or negative Θ branches of the buckled state connected to the compression branch. There is no significant difference in patterns observed in imperfect columns compared to post-buckling patterns seen in the perfect columns, with small (random) perturbations favouring one type of the pattern over another in any given compression run. However, both states are observed experimentally and in numerics with imperfect columns with approximately equal frequency (see also the faint markers in Fig. 3b).

4.2. Buckling threshold and post-buckling behaviour

The level of agreement between experiments and theory, demonstrated in Fig. 3a for the force–strain curves of columns with $N = 13$ holes, was also seen for columns with a different number of holes. This is shown in Fig. 4 by plotting the peak force, F_{cr}, and the corresponding compressive strain, ε_{cr}, and the slope of the force–strain curve beyond the critical compressive strain, $\partial F/\partial\varepsilon$, obtained experimentally and using the model with imperfect columns, as a function of the number of holes N in the holey column. When extracting slope values, we fitted a straight line
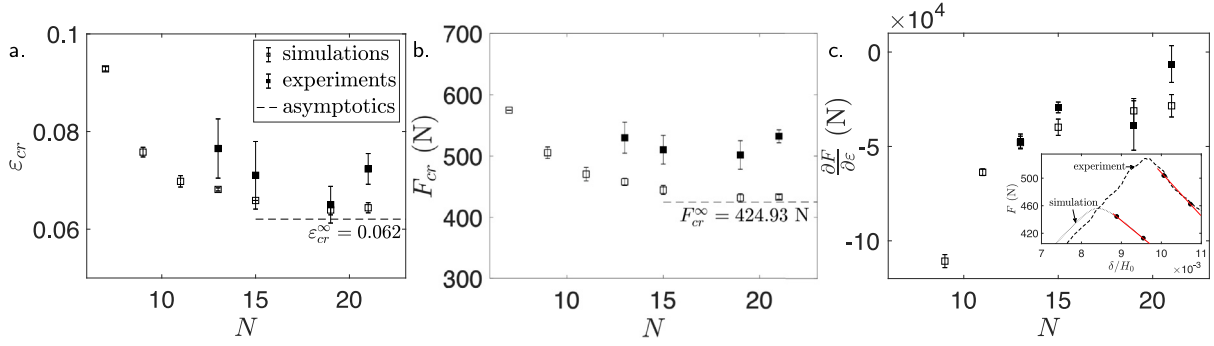
Fig. 4. Threshold for the onset of buckling and post-buckling behaviour. Critical: a. strain ε_{cr} and b. force F_{cr} for the onset of buckling; and c. post-buckling slope of the force–strain curve $\partial F / \partial \varepsilon$ in hard, holey columns measured both experimentally (filled markers) and via simulations using imperfect columns (unfilled markers) as a function of the number of holes N. The inset in c. shows the region of the force–strain curve (between two dots) where the slope $\partial F / \partial \varepsilon$ is sampled, using $N = 13$ as an example. For long columns, $N \gtrsim 15$, the macromechanical conditions for buckling become independent of the number of holes, approaching the theoretical limiting values of $\varepsilon_{cr}^{\infty} = 0.062$ and $F_{cr}^{\infty} = 424.93$ N (dashed lines).
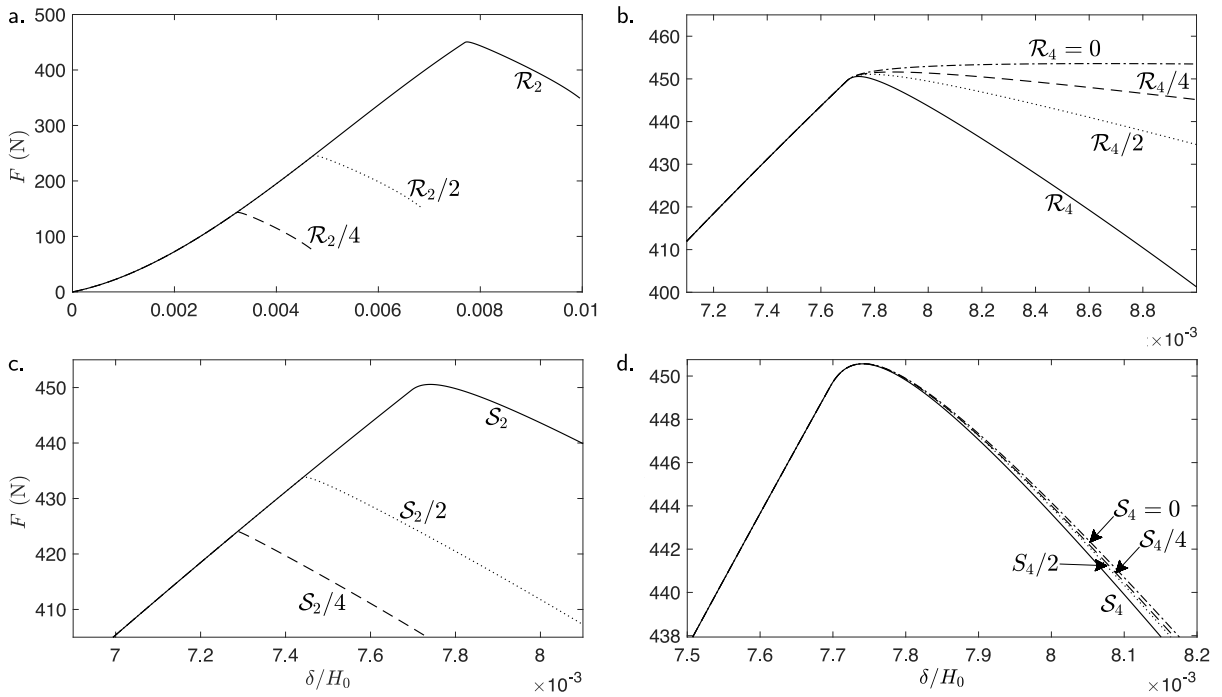

Fig. 5. The influence of micromechanical stiffness and constitutive nonlinearity on macromechanics. Force–strain curves for holey columns with $N = 13$ holes and varying: a. rotational stiffness $\mathcal{R}_2$; b. rotational nonlinearity $\mathcal{R}_4$; c. shear stiffness $\mathcal{S}_2$ and d. shear nonlinearity $\mathcal{S}_4$, with their reference magnitudes given in Section 2.1.

to the force–displacement measurements over a range of 0.05–0.07 mm in displacement beyond the critical value (an example of this fitting procedure for typical experimental and numerical data, respectively, is shown in the inset of Fig. 4c, where the dots signify the regions where the fitting was performed). The quantity $\partial F / \partial \varepsilon$ is then extracted using the slope of the straight line. The theoretical and experimental data is reported by averaging the results for 50 imperfect columns and five experimental samples, respectively, with the error on each point corresponding to the standard deviation of the data. As N increases, so does $\partial F / \partial \varepsilon$, i.e., post-buckling softening becomes weaker. On the other hand, both F_{cr} and ε_{cr} decrease with N approaching limiting values F_{cr}^{∞} and $\varepsilon_{cr}^{\infty}$, respectively. They correspond the threshold for the localised buckling in an infinite holey column: the force can be found using

$$F_{cr}^{\infty} = 4 \times 3 \times \frac{\mathcal{R}_2}{l}, \tag{33}$$

see [10,20], and the stress $\varepsilon_{cr}^{\infty}$ obtained by solving the implicit Eq. (2) with this value of the force.

4.3. The role of rotation and shearing

4.3.1. Nonlinear rotation

The importance of ligament bending stiffness and nonlinearity is demonstrated by varying coefficients $\mathcal{R}_2$ and $\mathcal{R}_4$ in (5) (Fig. 5a,b). As before, we focus on the force–strain curves for the perfect holey column with $N = 13$ holes.

In the limiting case of an infinite column, the magnitude of $\mathcal{R}_2$ determines the peak force and strain, the former being exactly proportional to $\mathcal{R}_2$ (33). The column with $N = 13$ holes behaves similarly, with the critical force changing approximately by a factor of two with each doubling of the coefficient $\mathcal{R}_2$ (Fig. 5a). However, the post-bifurcation stiffness (the slope of the force–displacement curve) does not change dramatically with variation of $\mathcal{R}_2$. Instead, the degree of post-bifurcation softening

is significantly controlled by $\mathcal{R}_4$, the coefficient resulting from constitutive nonlinearity in ligament bending (Fig. 5b). In the case of $\mathcal{R}_4 = 0$, the behaviour of the linear constitutive response is recovered, and no softening is observed. Similarly, there is no significant post-bucking softening in comparable hyperelastic columns [19], further demonstrating the importance of constitutive nonlinearities in rotation for the global response of holey columns.

4.3.2. Nonlinear shearing

For a given displacement, the forces measured in the shearing experiments with individual structural elements in Fig. 3c are larger than the corresponding rotational forces in Fig. 3d by a factor of 10, resulting in significantly greater energy penalty to shearing deformations. Thus, the deformations occurring during buckling are primarily rotational, but the shear deformation of ligaments, parameterised by $\mathcal{S}_2$ and $\mathcal{S}_4$ from (3) also affects the behaviour of holey columns with finite number of holes (Fig. 5c, d). For example, variations in $\mathcal{S}_2$ have a weak influence on the peak force, which for $N = 13$ holes decreases by less than 5% when $\mathcal{S}_2$ is changed by a factor of 2 (Fig. 5c). As in the case of rotational response, the post-bifurcation behaviour of the columns is largely unaffected by $\mathcal{S}_2$, but is dependent on S_4 (Fig. 5d), though this dependence is much less pronounced than the dependence on rotational nonlinearity R_4.

Overall, the results in Fig. 5 clearly demonstrate the need for modelling both linear and nonlinear responses of individual structural elements to different modes of deformation, emphasising in particular the importance of nonlinear terms for the post-buckling behaviour of hard holey columns.

5. Conclusion

By linking the micromechanics of ligaments to compression, shear and rotation with the macro-deformation of holey columns under compressive load, we have demonstrated how constitutive nonlinearities in individual structural elements translate to the global response of this particular mechanical metamaterial. This was done by building a modelling framework which was underpinned by experiments designed to quantify the micromechanical response. Our model was then tested by comparison with experiments on holey columns made from PLA plastic, a material with nonlinear constitutive behaviour, as evidenced by nonlinear response of the metamaterial under compression even prior to its buckling.

While the pattern transition studied in this paper is very robust, i.e., it occurs for perforated sheets and columns made from a range of materials including viscoelastic fluids [14], rubbers [13] or even metals [10], we clearly demonstrated the need for accurately quantifying the constitutive properties of such materials in order to predict the behaviour of holey structures quantitatively. In our study, both the onset of buckling (the critical strain at which it occurs) and the post-buckling behaviour of holey columns (force–strain curves) are strongly affected by material nonlinearities. Hence, tuning nonlinear constitutive response of structural elements in holey columns can also be used to adjust their global properties, such as the level of softening after buckling.

Our holey columns are particularly sensitive to the response of the microarchitecture to rotational deformation, which has strong influence on the level of agreement between our simulations and experiments in Figs. 3 and 4, though in columns of finite length made from different materials this might be less pronounced. Geometric imperfections, on the other hand, had relatively little quantitative effect on the global response of the system. Our finding illustrates why accurately quantifying responses of individual structural elements to the standard modes of deformation

is crucial for the predictive capabilities of modelling frameworks such as the one presented here, or in [22]. When quantifying these responses, we have chosen the simplest forms of nonlinearities (i.e. polynomials) that fitted our experimental data. The motivation behind such empirical approach was to use simple mathematical expressions which are nevertheless asymptotically valid, for example, in the limit of infinite columns with big holes [20]. For structural elements with more complicated shapes decoupling compressive, shear and rotational responses might not be as easy. However, the modelling approach taken here is an excellent starting point for exploring the role of constitutive nonlinearities in metamaterials of the same class as holey columns.

Declaration of competing interest

The authors declare that they have no known competing financial interests or personal relationships that could have appeared to influence the work reported in this paper.

Data availability

Data will be made available on request

Acknowledgements

References

[1] D.M.J. Dykstra, J. Busink, B. Ennis, C. Coulais, Viscoelastic snapping metamaterials, J. Appl. Mech. 86 (11) (2019) 111012.

[2] D.M.J. Dykstra, S. Janbaz, C. Coulais, The extreme mechanics of viscoelastic metamaterials, APL Mater. 10 (8) (2022) 080702.

[3] K. Che, M. Rouleau, J. Meaud, Temperature-tunable time-dependent snapping of viscoelastic metastructures with snap-through instabilities, Extreme Mech. Lett. 32 (2019) 100528.

[4] A. Souto, J. Zhang, A.M. Aragón, K.P. Velikov, C. Coulais, Edible mechanical metamaterials with designed fracture for mouthfeel control, Soft Matter 18 (2022) 2910–2919.

[5] P. Sehgal, M. Ramaswamy, E.Y.X. Ong, C. Ness, I. Cohen, B.J. Kirby, Viscosity metamaterials, 2022.

[6] H. Kocharyan, N. Karanjgaokar, Development of adaptive granular metamaterials for impact mitigation, Extreme Mech. Lett. 58 (2023) 101943.

[7] P. Qiao, M. Yang, F. Bobaru, Impact mechanics and high-energy absorbing materials: Review, J. Aerosp. Eng. 21 (2008).

[8] J. Brennan-Craddock, D. Brackett, R. Wildman, R. Hague, The design of impact absorbing structures for additive manufacture, J. Phys. Conf. Ser. 382 (2012) 012042.

[9] C.R. Calladine, R.W. English, Strain-rate and inertia effects in the collapse of two types of energy-absorbing structure, Int. J. Mech. Sci. 26 (1984) 689–701.

[10] F. Box, C.G. Johnson, D. Pihler-Puzović, Hard auxetic metamaterials, Extreme Mech. Lett. 40 (2020) 100980.

[11] K. Bertoldi, P.M. Reis, S. Willshaw, T. Mullin, Negative Poisson's ratio behaviour induced by an elastic instability, Adv. Mater. 22 (2010) 361–366.

[12] T. Mullin, S. Deschanel, K. Bertoldi, M.C. Boyce, Pattern transformation triggered by deformation, Phys. Rev. Lett. 99 (2007) 084301.

[13] K. Bertoldi, M.C. Boyce, S. Seschanel, S.M. Prange, T. Mullin, Mechanics of deformation-triggered pattern transformations and superelastic behavior in periodic elastomeric structures, J. Mech. Phys. Solids 56 (2008) 2642–2668.

[14] T. Mullin, S. Willshaw, F. Box, Pattern switching in soft cellular solids under compression, Soft Matter 9 (2013) 4951.

[15] F. Box, R. Bowman, T. Mullin, Dynamic compression of elastic and plastic cellular solids, Appl. Phys. Lett. 103 (2013) 151909.

[16] B. Florijn, C. Coulais, M. van Hecke, Programmable mechanical metamaterials, Phys. Rev. Lett. 113 (2014) 175503.

[17] C. Coulais, J.T.B. Overvelde, L.A. Lubbers, K. Bertoldi, M. van Hecke, Discontinuous buckling of wide beams and metabeams, Phys. Rev. Lett. 115 (2015) 044301.

[18] B. Florijn, C. Coulais, M. van Hecke, Programmable mechanical metamaterials: the role of geometry, Soft Matter 12 (2016) 8736–8743.

[19] D. Pihler-Puzović, A.L. Hazel, T. Mullin, Buckling of a holey column, Soft Matter 12 (2016) 7112.

[20] C.G. Johnson, U. Jain, A.L. Hazel, D. Pihler-Puzović, T. Mullin, On the buckling of an elastic holey column, Proc. R. Soc. Lond. Ser. A Math. Phys. Eng. Sci. 473 (2017) 20170477.

[21] K. Bertoldi, Harnessing instabilities to design tunable architectured cellular materials, Ann. Rev. Mater. Res. 47 (2017) 51–61.

[22] C. Coulais, C. Kettenis, M. van Hecke, A characteristic length scale causes anomalous size effects and boundary programmability in mechanical metamaterials, Nat. Phys. 14 (2018) 40–44.

[23] T.A.M. Hewage, K.L. Alderson, A. Alderson, F. Scarpa, Double-negative mechanical metamaterials displaying simultaneous negative stiffness and negative Poisson's ratio properties, Adv. Mater. 28 (46) (2016) 10323–10332.

[24] R. Gao, S. Guo, X. Tian, S. Liu, A negative-stiffness based 1D metamaterial for bidirectional buffering and energy absorption with state recoverable characteristic, Thin-Walled Struct. 169 (2021) 108319.

[25] Z. Nicolaou, A. Motter, Mechanical metamaterials with negative compressibility transitions, Nat. Mater. 11 (2012) 608–613.

[26] X. Tan, S. Chen, B. Wang, J. Tang, L. Wang, S. Zhu, K. Yao, P. Xu, Real-time tunable negative stiffness mechanical metamaterial, Extreme Mech. Lett. 41 (2020) 100990.

[27] X. Tan, B. Wang, S. Zhu, S. Chen, K. Yao, P. Xu, L. Wu, Y. Sun, Novel multidirectional negative stiffness mechanical metamaterials, Smart Mater. Struct. 29 (1) (2019) 015037.

[28] Y.-C. Wang, R.S. Lakes, Negative stiffness-induced extreme viscoelastic mechanical properties: stability and dynamics, Phil. Mag. 84 (35) (2004) 3785–3801.

[29] Y.-C. Wang, R.S. Lakes, Stable extremely-high-damping discrete viscoelastic systems due to negative stiffness elements, Appl. Phys. Lett. 84 (22) (2004) 4451–4453.

[30] T. Jaglinski, D. Kochmann, D. Stone, R.S. Lakes, Composite materials with viscoelastic stiffness greater than diamond, Science 315 (5812) (2007) 620–622.

[31] D.M. Kochmann, Stable extreme damping in viscoelastic two-phase composites with non-positive-definite phases close to the loss of stability, Mech. Res. Commun. 58 (2014) 36–45.

[32] C. Morris, L. Bekker, C. Spadaccini, M. Haberman, C. Seepersad, Tunable mechanical metamaterial with constrained negative stiffness for improved quasi-static and dynamic energy dissipation, Adv. Eng. Mater. 21 (7) (2019) 1900163.

[33] T. Klatt, M.R. Haberman, A nonlinear negative stiffness metamaterial unit cell and small-on-large multiscale material model, J. Appl. Phys. 114 (3) (2013) 033503.

[34] B. Deng, J.R. Raney, V. Tournat, K. Bertoldi, Elastic vector solitons in soft architected materials, Phys. Rev. Lett. 118 (20) (2017) 204102.

[35] X. Xia, C.M. Spadaccini, J.R. Greer, Responsive materials architected in space and time, Nat. Rev. Mater. 7 (2022) 683–701.

[36] D. Pasini, J.K. Guest, Imperfect architected materials: mechanics and topology optimization, MRS Bull. 44 (2019) 766–772.